

# Significant wintertime PM<sub>2.5</sub> mitigation in the Yangtze River Delta, China from 2016 to 2019: observational constraints on anthropogenic emission controls

Liqiang Wang<sup>1</sup>, Shaocai Yu<sup>\*,1,2</sup>, Pengfei Li<sup>\*,3,1</sup>, Xue Chen<sup>1</sup>, Zhen Li<sup>1</sup>, Yibo Zhang<sup>1</sup>, Mengying Li<sup>1</sup>, Khalid Mehmood<sup>1</sup>, Weiping Liu<sup>1</sup>, Tianfeng Chai<sup>4</sup>, Yannian Zhu<sup>5</sup>, Daniel Rosenfeld<sup>6</sup>, and John H. Seinfeld<sup>2</sup>

<sup>1</sup>Research Center for Air Pollution and Health; Key Laboratory of Environmental Remediation and Ecological Health, Ministry of Education, College of Environment and Resource Sciences, Zhejiang University, Hangzhou, Zhejiang 310058, P.R. China

<sup>2</sup>Division of Chemistry and Chemical Engineering, California Institute of Technology, Pasadena, CA 91125, USA

<sup>3</sup>College of Science and Technology, Hebei Agricultural University, Baoding, Hebei 071000, P.R. China

<sup>4</sup>Air Resources Laboratory, NOAA, Cooperative Institute for Satellite Earth System Studies (CISESS), University of Maryland, College Park, USA

<sup>5</sup>Meteorological Institute of Shanxi Province, 36 Beiguangzhengjie, Xi'an 710015, China

<sup>6</sup>Institute of Earth Science, The Hebrew University of Jerusalem, Jerusalem, Israel

Correspondence to: Shaocai Yu (shaocaiyu@zju.edu.cn); Pengfei Li (lpf\_zju@163.com)

To be submitted to

Atmospheric Chemistry and Physics

## 26 **ABSTRACT**

27 Ambient fine particulate matter (PM<sub>2.5</sub>) mitigation relies strongly on anthropogenic emission control measures, the actual  
28 effectiveness of which is challenging to pinpoint owing to the complex synergies between anthropogenic emissions and  
29 meteorology. Here, observational constraints on model simulations allow us to derive not only reliable PM<sub>2.5</sub> evolution but  
30 also accurate meteorological fields. On this basis, we isolate meteorological factors to achieve reliable estimates of surface  
31 PM<sub>2.5</sub> responses to both long-term and emergency emission control measures from 2016 to 2019 over the Yangtze River Delta  
32 (YRD), China. The results show that long-term emission control strategies play a crucial role in curbing PM<sub>2.5</sub> levels, especially  
33 in the megacities and other areas with abundant anthropogenic emissions. The G20 summit hosted in Hangzhou in 2016  
34 provides a unique and ideal opportunity involving the most stringent, even unsustainable, emergency emission control  
35 measures. The most substantial declines in PM<sub>2.5</sub> concentrations ( $\sim 35 \mu\text{g}/\text{m}^3$ ,  $\sim 59\%$ ) are achieved in Hangzhou and its  
36 surrounding areas. The following hotspots also emerge in megacities, especially in Shanghai ( $32 \mu\text{g}/\text{m}^3$ , 51%), Nanjing ( $27$   
37  $\mu\text{g}/\text{m}^3$ , 55%), and Hefei ( $24 \mu\text{g}/\text{m}^3$ , 44%). Compared to the long-term policies from 2016 to 2019, the emergency emission  
38 control measures implemented during the G20 Summit achieve more significant decreases in PM<sub>2.5</sub> concentrations ( $17 \mu\text{g}/\text{m}^3$   
39 and 41%) over most of the whole domain, especially in Hangzhou ( $24 \mu\text{g}/\text{m}^3$ , 48%) and Shanghai ( $21 \mu\text{g}/\text{m}^3$ , 45%). By  
40 extrapolation, we derive insight into the magnitude and spatial distribution of PM<sub>2.5</sub> mitigation potential across the YRD,  
41 revealing significantly additional room for curbing PM<sub>2.5</sub> levels.

## 42 **1 INTRODUCTION**

43 Anthropogenic induced fine particulate matter (particulate matter with an aerodynamic diameter smaller than  $2.5 \mu\text{m}$ ,  
44 hereinafter denoted as PM<sub>2.5</sub>) is a principal object of air pollution control in China (Huang et al., 2014; Zhang et al., 2015).  
45 Moreover, the government has made major strides in curbing anthropogenic emissions (e.g., SO<sub>2</sub>, NO<sub>x</sub>, and CO) via both long-  
46 term and emergency measures during the past decade (Yan et al., 2018; Yang et al., 2019; Zhang et al., 2012). However, owing  
47 to the complex synergy of chemistry and meteorology (Seinfeld and Pandis, 2016), the extent to which these measures have  
48 abated PM<sub>2.5</sub> pollution, as well as the attainable mitigation potential, remains unclear (An et al., 2019).  
49 The main challenge involves reliably representing substantial and rapid changes in anthropogenic emissions resulting from  
50 both long-term and emergency control measures (Chen et al., 2019; Cheng et al., 2019; Zhang et al., 2014; Yang et al., 2016;  
51 Zhai et al., 2019; Zhang et al., 2019; Zhong et al., 2018). To gain timely insight into variations in anthropogenic emissions,  
52 considerable efforts went into establishing detailed bottom-up emissions and derived valuable findings (Cheng et al., 2019;  
53 Zhang et al., 2019). Yet bottom-up inventories were built on the basis of activity data as well as emission factors. These input  
54 data can be absent or outdated, likely leading to misunderstandings of anthropogenic impacts, particularly in terms of the

55 magnitude (Jiang et al., 2018). Recent studies applied available observations to construct multilinear regression models  
56 (emission-based or meteorology-related), thus allowing us to separate contributions from anthropogenic emissions and  
57 meteorology to some extent (Zhai et al., 2019; Zhong et al., 2018). However, the uncertainties in bottom-up inventories and  
58 meteorology remained. Here we switched to observational constraints on a state-of-the-art chemical model. This can be a  
59 potential way to tackle this challenge.

60 Since 2013, the China National Environmental Monitoring Center (CNEMC) has established 1415 ground-based  $\text{PM}_{2.5}$   
61 measurement sites across 367 key cities (Zhang and Cao, 2015). In contrast to satellite observations with sparse spatiotemporal  
62 coverages (Ma et al., 2014, 2015; Xue et al., 2019), these ground sites can provide hourly  $\text{PM}_{2.5}$  concentrations at high spatial  
63 resolution in urban areas. Data assimilation (DA) methods that have been widely used in meteorology can be extended to  
64 integrate those continuous observational constraints with chemical transport models (CTMs) (Bocquet et al., 2015; Chai et al.,  
65 2017; Gao et al., 2017; Jung et al., 2019; Ma et al., 2019). It has been demonstrated that the capability of several representative  
66 DA methods, such as the optimal interpolation (OI) (Chai et al., 2017), 3D/4D variational methods (Li et al., 2016), and the  
67 ensemble Kalman filter algorithm (Chen et al., 2019), can bridge the estimation gaps between observed and simulated results.  
68 Thus, observational constraints can be taken full advantage of to identify the effects of anthropogenic emission controls.

69 From the perspective of policymaking, 2016 was a special year for air pollution control in China. Since 2013, the Chinese  
70 government instituted extensive policies, such as the Air Pollution Prevention and Control Action Plan. These strategies were  
71 initiated and implemented through generally shutting down or relocating high emission traditional industrial enterprises  
72 (Sheehan et al., 2014; Shi et al., 2016; Xie et al., 2015). Starting from January 1, 2016, the relevant law, as well as the “Blue  
73 Sky Battle Plan”, came into full effect and profoundly shifted how China prioritized air quality management (Feng and Liao,  
74 2016; Li et al., 2019c). Hence, we address the impact of long-term emission control strategies on  $\text{PM}_{2.5}$  mitigation from 2016  
75 onward.

76 The G20 summit hosted in Hangzhou in 2016 (hereinafter termed the G20 summit) provides a unique and ideal opportunity to  
77 further explore the attainable  $\text{PM}_{2.5}$  mitigation potential across the Yangtze River Delta (YRD) (Li et al., 2017c; Ma et al.,  
78 2019; Shu et al., 2019; Yang et al., 2019). Prior to and during this period, the Chinese government enforced historically strictest,  
79 even unsustainable, emergency emission control measures, including significant control, even cessation, of factory operations,  
80 restrictions on vehicles in the region, thus achieving significant  $\text{PM}_{2.5}$  abatement at specific locations (e.g., Hangzhou) (Ji et  
81 al., 2018; Li et al., 2017c; Yang et al., 2019). Those measures were conducted across the whole YRD (including Zhejiang,  
82 Jiangsu, and Anhui provinces, and Shanghai municipality), particularly in Hangzhou that served as the host city (Li et al.,  
83 2019b, 2017c; Ni et al., 2020; Yu et al., 2018). Li et al. (2017) assumed that most of anthropogenic emissions (e.g., those from  
84 industry, power plant, residential, and on-road transportation sectors) were reduced by around 50%. The role of these

85 emergency emission control measures, that is, the relatively localized PM<sub>2.5</sub> mitigation potential, can thus be identified, and  
86 further extended to the entire YRD.  
87 To quantify the effectiveness of the emission control strategies, we constrained a state-of-the-art CTM by a reliable DA method  
88 with extensive chemical and meteorological observations. This comprehensive technical design provides a crucial advance in  
89 isolating the influences of emission changes and meteorological perturbations over the YRD from 2016 to 2019, thus deriving  
90 estimates of PM<sub>2.5</sub> responses to both long-term and emergency emission control measures, and establishing the first map of  
91 the PM<sub>2.5</sub> mitigation potential across the YRD.

## 92 **2 MATERIALS AND METHODS**

### 93 **2.1 The two-way coupled WRF-CMAQ model**

94 The two-way coupled Weather Research and Forecasting (WRF) and Community Multiscale Air Quality (CMAQ) model (the  
95 WRF-CMAQ model), as the key core of the DA system, was applied to investigate the ambient PM<sub>2.5</sub> feedbacks under different  
96 constraining circumstances (Byun and Schere, 2006; Wong et al., 2012; Yu et al., 2013). We utilized the CB05 and AERO6  
97 modules for gas-phase chemistry and aerosol evolution (Carlton et al., 2010; Yarwood et al., 2005), respectively. Both  
98 secondary inorganic and organic aerosol (i.e., SIA and SOA) were thus explicitly treated with the AERO6 scheme in the WRF-  
99 CMAQ model. Together with the ISORROPIA II thermodynamic equilibrium module (Fountoukis and Nenes, 2007), SIA in  
100 the Aitken and accumulation modes (Binkowski and Roselle, 2003) was assumed to be in thermodynamic equilibrium with  
101 the gas phase, while that in the coarse mode was treated dynamically. SOA was formed via gas-, aqueous-, and aerosol-phase  
102 oxidation processes, such as in-cloud oxidation of glyoxal and methylglyoxal, absorptive partitioning of condensable oxidation  
103 of monoterpenes, long alkanes, low-yield aromatic products (based on m-xylene data), and high-yield aromatics, and NO<sub>x</sub>-  
104 dependent yields from aromatic compounds (Carlton et al., 2010). The subsequent reaction products can be divided into two  
105 groups: non-volatile semi-volatile. Such treatments have been widely used and comprehensively validated. Longwave and  
106 shortwave radiation were both treated using the RRTMG radiation scheme (Clough et al., 2005). Related land surface energy  
107 balance and planetary boundary layer simulations were included in the Pleim-Xiu land surface scheme (Xiu and Pleim, 2001)  
108 and the asymmetric convective model (Pleim, 2007b, 2007a), respectively. The two-moment Morrison cloud microphysics  
109 scheme (Morrison and Gettelman, 2008) and the Kain-Fritsch cumulus cloud scheme (Kain, 2004) were employed for  
110 simulating aerosol-cloud interactions and precipitation. Default settings in the model were used to prescribe chemical initial  
111 and boundary conditions. A spin-up period of seven days was carried out in advance to eliminate artefacts associated with  
112 initial conditions. Meteorological initial and boundary conditions were obtained from the ECMWF reanalysis dataset with the  
113 spatial resolution of 1° × 1° and temporal resolution of 6 hours (<http://www.ecmwf.int/products/data>, last access: 7 March

2020). Biogenic and dust emissions were calculated on-line using the Biogenic Emission Inventory System version 3.14 (BEISv3.14) (Carlton and Baker, 2011) and a windblown dust scheme embedded in CMAQ (Choi and Fernando, 2008), respectively.

The horizontal domain of the model covered mainland China by a  $395 \times 345$  grid with a 12 km horizontal resolution following a Lambert Conformal Conic projection (Figure 1). In terms of the vertical configuration, 29 sigma-pressure layers ranged from the surface to the upper level pressure of 100 hPa, 20 layers of which are located below around 3 km to derive finer meteorological and chemical characteristics within the planetary boundary layer.

As a state-of-the-art CTM, the WRF-CMAQ model has been widely used to simulate spatiotemporal  $PM_{2.5}$  distributions at regional scales. However, model biases remain, mainly due to imperfect representations of chemical and meteorological processes. Inaccurate anthropogenic emissions will exacerbate these biases. Therefore, external constraints on simulated results enforced by the DA method will be taken into account in order to optimize spatiotemporal  $PM_{2.5}$  distributions (Bocquet et al., 2015).

## 2.2 Anthropogenic emissions

The anthropogenic emissions were obtained from the Multi-resolution Emission Inventory for China version 1.2 (MEIC)(Li et al., 2017b), which contained primary species (e.g., primary  $PM_{2.5}$ ,  $SO_2$ ,  $NO_x$ , CO, and  $NH_4$ ) from five anthropogenic sectors (i.e., agriculture, power plant, industry, residential, and transportation). This inventory was initially designed with the spatial resolution of  $0.25^\circ \times 0.25^\circ$  and thus needed to be reallocated to match the domain configuration (i.e.,  $12km \times 12km$ ) in the study.

Recent findings show that MEIC generally provides reasonable estimates of total anthropogenic emissions for several typical regions in China, such as the Beijing-Tianjin-Hebei region, the YRD, and the Pearl River Delta region (Li et al., 2017b). Nevertheless, large uncertainties in spatial proxies (e.g., population density and road networks) still exist within these specific regions (Geng et al., 2017). More, MEIC was originally constructed for the 2016 base year. Hence, owing to the impact of the long-term emission control measures, MEIC was considered to be inappropriate for this study period (i.e., 2019). Comparatively, emergency control measures could give rise to much more significant emission controls in the short term, thereby leading to further uncertainties.

## 2.3 Observational network

To track real-time air quality in China, the National Environmental Monitoring Center (CNEMC, <http://www.cnemc.cn/>, last access: 7 March 2020) has established 1415 sites across 367 cities since 2013 (Figure 1). Among these, 244 monitoring sites were densely distributed in 6660 grid cells across the YRD providing hourly  $PM_{2.5}$  measurements, resulting in potentially

143 excellent roles in constraining simulated PM<sub>2.5</sub> (Bocquet et al., 2015). In this study, we applied observed PM<sub>2.5</sub> concentrations  
 144 to constrain and evaluate the model performance. It is worth noting that the constraining capability of those observations varies  
 145 depending on specific configurations (e.g., the nature of the utilized DA method, the assimilation frequency, and the  
 146 representative errors of observations) (Bocquet et al., 2015; Chai et al., 2017; Ma et al., 2019; Rutherford, 1972). As shown in  
 147 Figure 1a, to consider regional impacts outside the YRD, the ground-level observations in the fan-shaped quadrilateral were  
 148 used to constrain the model performance. This was mainly due to the fact that this fan-shaped geographical scope covered  
 149 almost all key regions that had potentially regional impacts on the YRD, involving the Beijing-Tianjin-Hebei region (BTH),  
 150 the Pearl River Delta region, the Sichuan-Chongqing region, and the Shaanxi-Gansu region (Zhang et al., 2019). On the other  
 151 hand, the ground monitoring sites within the fan-shaped quadrilateral were significantly denser than those outside, thus leading  
 152 to much more effective DA results in practice (Bocquet et al., 2015; Chai et al., 2017). Collectively, to assimilate the  
 153 observations in the fan-shaped quadrilateral might be a sensible way to balance the DA effectiveness and the computing  
 154 efficiency. A resultant evidence lies in the model performance evaluation in Sect. 3.1, which would prove that this DA  
 155 configuration can enable reliable PM<sub>2.5</sub> simulations.

## 156 2.4 Optimal interpolation

157 Optimal interpolation (OI) was chosen to assimilate hourly observations into the WRF-CMAQ model, aiming to generate the  
 158 accurate state of spatiotemporal PM<sub>2.5</sub> distributions. Compared to the solely model-dependent results, this constraining method  
 159 relies on observations and thus makes it possible to minimize model uncertainties in optimizing the spatiotemporal PM<sub>2.5</sub>  
 160 changes resulting from emission controls (Chai et al., 2017; Jung et al., 2019). The analysed states from the OI method were  
 161 calculated based on the following interpolation equation:

$$162 \quad \mathbf{X}^a = \mathbf{X}^b + \mathbf{B}\mathbf{H}^T(\mathbf{H}\mathbf{B}\mathbf{H}^T + \mathbf{O})^{-1}(\mathbf{Y} - \mathbf{H}\mathbf{X}^b) \quad (1)$$

163 where  $\mathbf{X}^a$  and  $\mathbf{X}^b$  denote the analysis (constrained) and background (simulated) values, respectively.  $\mathbf{B}$  and  $\mathbf{O}$  are background  
 164 and observation error-covariance matrices, respectively, for which we assumed no correlation in this study.  $\mathbf{H}$  refers to a  
 165 linearized observational operator, and  $\mathbf{Y}$  represents the observation vector. The OI method is described in detail in Adhikary  
 166 et al. (Adhikary et al., 2008).

167 Once available measurements were assimilated, the states of the simulated variables were adjusted from their background  
 168 values to corresponding analysis states using the scaling ratio  $\mathbf{X}^a/\mathbf{X}^b$  obtained following equation (1). As the measurements  
 169 were conducted at the surface, this ratio at each grid cell was used to scale all aerosol components below the boundary layer  
 170 top. Such simplification compensated for the lack of information to constrain speciated aerosol components or their vertical  
 171 distributions. When ground-level PM<sub>2.5</sub> measurements were assimilated, hourly observations were put into equation (1) to  
 172 construct the new analysis fields. All-day state variables associated with aerosols in the model were adjusted from their

background (simulated) to their analysis (constrained) states using the scaling factors ( $\mathbf{X}^a/\mathbf{X}^b$ ). The adjusted model state variables were then used to initiate the model to predict the next background state ( $\mathbf{X}^b$ ) in Equation (1). Therefore, the background state ( $\mathbf{X}^b$ ) served as a prior model prediction before it was combined with the newly available observation ( $\mathbf{Y}$ ) to generate a new analysis state ( $\mathbf{X}^a$ ) using Equation (1). Measurements within the background-error correlation length scale were used to shape analysis states ( $\mathbf{X}^a$ ). The background error covariance  $\mathbf{COV}_{ij}$  between any two grid cells  $i$  and  $j$  was simulated as

$$\mathbf{COV}_{ij} = \boldsymbol{\varepsilon}_i \boldsymbol{\varepsilon}_j e^{-\frac{\Delta_{ij}}{L}} \quad (2)$$

where  $\boldsymbol{\varepsilon}_i$  and  $\boldsymbol{\varepsilon}_j$  referred to the standard deviations of the background errors in two grid cells and  $\Delta_{ij}$  denoted the distance between the two grids. As a result,  $L$  was the background-error correlation length scale, which can be obtained by the Hollingsworth-Lönnberg method (Chai et al., 2017; Hollingsworth and Lönnberg, 1986; Kumar et al., 2012). Figure 2 shows the correlation coefficient, i.e.,  $\mathbf{COV}_{ij}/\boldsymbol{\varepsilon}_i \boldsymbol{\varepsilon}_j$ , as a function of the separation distance between two grid cells, which was averaged over 10 km bins. The results identified that a correlation length scale of  $\sim 180$  km could be treated as the threshold. It allowed the correlation coefficients to fall within the range of  $e^{-1}$ , defining the effective radius of each individual observation. Due to the intensive monitoring sites in our study domain, this threshold was applied uniformly for the YRD. In this study, observations beyond the background-error correlation length scale would have no effect on  $\mathbf{X}^a$ . Following Chai et al. (Chai et al., 2017), the standard deviation of the background errors was assigned as 60% of the background values, while the observational errors were assumed to be  $\pm 20\%$  of the measurement values.

## 2.4 Experiment design

Anthropogenic emission controls and meteorological perturbations are both critical factors that dominate interannual and daily variations in ambient  $\text{PM}_{2.5}$  (Zhang et al., 2019). Our major objective is to isolate the impacts of emission-oriented long-term and emergency measures and further explore the attainable  $\text{PM}_{2.5}$  mitigation potential. We designed three sets of experiments, which focused on three time periods, January 2016, January 2019, and the G20 period (from August 26, 2016 to September 7, 2016), respectively (Table 1).

For all experiments, the anthropogenic emissions were kept consistent (i.e., MEIC), while the ECMWF reanalysis datasets accounted for the hourly observational constraints on spatiotemporal meteorological evolutions. The ECMWF reanalysis datasets accounted for the hourly observational constraints on spatiotemporal meteorological evolutions. Therein almost all necessary meteorological factors (nine variables), involving temperature, U wind component, V wind component, pressure, relative humidity, precipitation, short-wave radiation, cloud cover, and planetary boundary layer height (PBLH), were assimilated (<https://apps.ecmwf.int/datasets/data/interim-full-daily/levtype=sfc/>, last access: 7 March 2020). These

configurations unified both chemical (i.e., emission inventories) and meteorological input data for the WRF-CMAQ model. Hence, the extent to which we introduce observational constraints on simulated  $PM_{2.5}$  variations using the OI method is the key to isolate the impacts of anthropogenic emission controls. Specifically, the differences in the constrained  $PM_{2.5}$  concentrations between DA\_2016 and DA\_2019 reflected the net effects of anthropogenic emission controls and meteorological perturbations between 2016 and 2019, while meteorological impacts therein were calculated as the discrepancies in simulated  $PM_{2.5}$  concentrations between NO\_2016 and NO\_2019 (Chen et al., 2019). Hence, by subtracting meteorological impacts from the net effects, we can isolate the effects of anthropogenic emission controls attributable to the long-term strategies.

The G20 summit provided a unique opportunity to realize the  $PM_{2.5}$  mitigation potential in specific regions (Li et al., 2019a, 2017c; Ma et al., 2019; Shu et al., 2019; Yang et al., 2019). This is due to the fact that the Chinese government implemented the most historically stringent, even unsustainable, strategies to curb anthropogenic emissions during that period in Hangzhou and surrounding areas. To quantify the projected  $PM_{2.5}$  abatement, we adopted the abovementioned method to constrain the unique  $PM_{2.5}$  variations in the DA\_G20 experiment and further compared the corresponding results with those of the sole model-dependent analysis (i.e., NO\_G20). However, the subsequent discrepancies were related not only to the effects of emergency anthropogenic emission strategies but also to the inherent biases mainly due to the emission inventory (Zhang et al., 2019). In theory, such biases would generally remain unchanged in the short term when no emergency emission controls occurred. Their consequent impacts could thus be stable under similar meteorological conditions. Therefore, to avoid additional uncertainties, the adjacent periods of the G20 summit (i.e., pre- and post- periods, from August 11 to August 23, 2016 and from September 18 to September 30, 2016, respectively) are the optimal alternative to eliminate the impacts of those inherent biases. Figure S1 demonstrates the significantly similar meteorological fields among these three periods. As a result, the corresponding experiments (i.e., DA\_CON\_G20 and NO\_CON\_G20) (Table 1) were conducted. By subtracting such differences, we could isolate the  $PM_{2.5}$  responses to the solely emergency anthropogenic emission strategies and finally achieve the  $PM_{2.5}$  mitigation potential for specific locations. Such localized  $PM_{2.5}$  mitigation potential should be further expanded to the entire YRD based on the impacts of both long-term and emergency strategies.

There is an essential prerequisite to above analysis. As the evaluation protocols, we need to verify that the DA experiments (i.e., DA\_2016, DA\_2019, DA\_G20, and DA\_CON\_G20) can reproduce the spatiotemporal variations in the  $PM_{2.5}$  and major meteorological fields (i.e., temperature, relative humidity, wind speed and air pressure) (Chai et al., 2017). While 244 monitoring stations reside in 6660 grid cells, 16 grid cells have two to three monitors in them. For these grid cells, only one averaged measurement was used for DA. However, all the observations were compared against the constrained results. Although SIA and SOA are key components of the ambient  $PM_{2.5}$ , extensive measurements at the regional scale of these components are generally lacking. It is thus difficult to generate appropriate constraints on SIA and SOA (Chai et al., 2017;



233 Gao et al., 2017). Note that different anthropogenic emissions might lead to inconsistent estimation of meteorological effects  
234 on ambient PM<sub>2.5</sub> (Chen et al., 2019). To eliminate this doubt, we conducted sensitivity tests by reducing MEIC with three  
235 reasonable ratios (i.e., -5%, -25%, and -40%) over the YRD based on NO<sub>2016</sub> and NO<sub>2019</sub>.

236 **3 RESULTS**

237 **3.1 Data assimilation performance**

238 Figure 3 shows spatial comparisons of hourly averaged concentrations of constrained and simulated PM<sub>2.5</sub> (i.e., the ones from  
239 the cases with and without DA, respectively) with ground-level observations across the YRD for January 2016, January 2019,  
240 and the G20 summit. In the NO<sub>2016</sub>, NO<sub>2019</sub>, and NO<sub>G20</sub> experiments, the simulated PM<sub>2.5</sub> concentrations generally  
241 overestimated observed values by 16 ~ 57 µg/m<sup>3</sup>, especially those in Hangzhou and surrounding areas during the G20 summit  
242 (> 21 µg/m<sup>3</sup>). Such prevailing overestimates were mainly a result of the anthropogenic emission inventory (i.e., MEIC), as a  
243 bottom-up product, which notably cannot capture interannual emission changes since the base year 2012, as well as the large  
244 emission controls resulting from the emergency controls during the G20 summit. By comparison, the constrained results  
245 significantly approach observations. Specifically, in the DA<sub>2016</sub>, DA<sub>2019</sub>, and DA<sub>G20</sub> cases, the biases of the assimilated  
246 PM<sub>2.5</sub> were all constrained in an extremely narrow range (i.e., 10 µg/m<sup>3</sup>, 12 µg/m<sup>3</sup>, and 13 µg/m<sup>3</sup>, respectively), suggesting that  
247 the DA method can reproduce the spatiotemporal distributions of surface PM<sub>2.5</sub> at the regional scale.

248 To achieve more targeted evaluations, it is necessary to further assess the ability of the DA method in reproducing the city-  
249 level PM<sub>2.5</sub> responses. With the analysis of time series over the same periods, Figure 4 illustrates the comparisons between  
250 hourly observed, simulated, and constrained PM<sub>2.5</sub> concentrations over the whole domain and four representative cities (i.e.,  
251 Shanghai, Hangzhou, Nanjing, and Hefei). Similar to the spatial comparisons, the constrained PM<sub>2.5</sub> generally reproduces the  
252 temporal variations in observations, while the model-dependent simulated results are prone to overestimating those  
253 observations, in particular, the peaks by 85 ~ 257 µg/m<sup>3</sup>.

254 As expected, basic evaluation indicators (i.e., the NMB and R values) of assimilated PM<sub>2.5</sub> exhibited significantly better  
255 behaviour than those without constraints (Figure S2). Taking the simulated and assimilated results for Hangzhou during  
256 January 2016 as an example, the corresponding R values improved from 0.63 to 0.98, while the NMB values were reduced  
257 from 17% to 3%. Similar improvements, but with varying extent, were found in other paired experiments.

258 Owing to the fact that the distinct PM<sub>2.5</sub> levels might also play a potential role in the DA performance, we thus separated the  
259 entire range of the observed PM<sub>2.5</sub> concentrations into four intervals (i.e., < 35 µg/m<sup>3</sup>, 35 ~ 75 µg/m<sup>3</sup>, 75 ~ 115 µg/m<sup>3</sup>, and >  
260 115 µg/m<sup>3</sup>), exactly corresponding to the continuously increasing PM<sub>2.5</sub> levels. Figure S3 demonstrates that, relative to the sole  
261 model-dependent configurations, this constraining method could substantially strengthen the model performance, especially

for the relatively elevated concentration intervals. Overall, the ranges of the NMB values and associated standard deviations decreased from -24 ~ 86% to -9 ~ 25% and 34 ~ 174  $\mu\text{g}/\text{m}^3$  to 12 ~ 52  $\mu\text{g}/\text{m}^3$ , respectively. Theoretically, more frequent DA should lead to more robust simulations. Hourly observational constraints on the  $\text{PM}_{2.5}$  concentrations were thus adopted to tackle this issue. This is the reason why the corresponding NMB values in the constraining cases roughly maintain stability, fluctuating over a narrow range (i.e.,  $\pm 20\%$ ) in the study periods (Figure S4). In addition, given the fact that the assimilated ERA reanalysis dataset has much wider spatial coverage than ground-based measurements, we also reproduced the spatiotemporal variations in the meteorological factors (e.g., temperature, relative humidity, wind speed, and air pressure) (Figures S5 ~ S8). Together the comprehensive evaluation statistics as summarized in Tables S1 ~ S5, it has been demonstrated that the DA method can enable one to derive not only reliable  $\text{PM}_{2.5}$  evolution but also accurate meteorological fields. Regional transport of  $\text{PM}_{2.5}$  can thus be captured reasonably in this way.

### 3.2 Ambient $\text{PM}_{2.5}$ responses to the long-term strategies

The Chinese government has been implementing stringent emission control strategies since 2016, especially in the YRD (Feng and Liao, 2016; Li et al., 2019c). To quantify subsequent  $\text{PM}_{2.5}$  responses is thus the prerequisite to our final objective, that is, to explore the associated  $\text{PM}_{2.5}$  mitigation potential.

Interannual changes in spatiotemporal  $\text{PM}_{2.5}$  distributions depended strongly on both anthropogenic emission controls and meteorological variations from 2016 to 2019. Their combined effects were reflected by the differences between the constrained results from DA\_2016 and DA\_2019. As shown in Figure 5a, such net impacts led to prevailing  $\text{PM}_{2.5}$  abatement in the domain, especially in megacities, such as Shanghai (13  $\mu\text{g}/\text{m}^3$ , 21%), Hangzhou (13  $\mu\text{g}/\text{m}^3$ , 17%), Nanjing (6  $\mu\text{g}/\text{m}^3$ , 8%), and Hefei (2  $\mu\text{g}/\text{m}^3$ , 2%). In addition, noticeable  $\text{PM}_{2.5}$  controls also occurred in the western and northern YRD, where abundant anthropogenic emissions are concentrated (Figure S9). Detailed differences are shown in Table S6.

Figure 5b highlights that the sole meteorological interferences played an extensively positive role in increasing the regional  $\text{PM}_{2.5}$  concentrations for most areas of the domain ( $\sim 12 \mu\text{g}/\text{m}^3$ , 15%). This also indirectly implied the importance of assimilating meteorology, which, however, were generally neglected by previous studies (Chen et al., 2019). In this study, we have eliminated this speculation. As shown in Figure S10 and Figure 5, even with the largest adjustment (i.e., -40%), such interferences could be well controlled within the 5% ( $< 3 \mu\text{g}/\text{m}^3$ ) scope, let alone other tests (i.e.,  $< 3\%$ ,  $< 2 \mu\text{g}/\text{m}^3$ ). Moreover, these findings are consistent with previous analyses (Chen et al., 2019; Zhang et al., 2019). They generally reveal that reasonable changes in the bottom-up emissions, together with the same meteorology input data, would not remarkably alter the simulated results associated with meteorological effects on surface  $\text{PM}_{2.5}$  ( $< 5\%$ ). As a result, some past studies even directly ignored such sensitivity tests without any discussion (Chen et al., 2019). Therefore, by subtracting those meteorological influences from the combined outcomes, we can finally derive the contributions of anthropogenic emission

controls to the PM<sub>2.5</sub> mitigation at the regional scale. Figure 5c illustrates that long-term emission control strategies from 2016 to 2019 produced substantial ( $> 14 \mu\text{g}/\text{m}^3$ , 19%) decreases in regional PM<sub>2.5</sub> concentrations, which are similar to those combined effects in terms of the spatial distributions.

For the entire domain, as well as the four representative cities, the synergy between anthropogenic emission controls and meteorological interferences on the PM<sub>2.5</sub> concentrations were calculated at the city level (Figure 6). We found that their net effects resulted in uniformly positive mitigations as follows:  $-2 \mu\text{g}/\text{m}^3$  (-3%),  $-13 \mu\text{g}/\text{m}^3$  (-21%),  $-12 \mu\text{g}/\text{m}^3$  (-17%),  $-6 \mu\text{g}/\text{m}^3$  (-8%), and  $-2 \mu\text{g}/\text{m}^3$  (-3%) for the whole domain, Shanghai, Hangzhou, Nanjing, and Hefei, respectively, while the meteorological conditions therein offset such effects to different extents ( $5 \sim 18 \mu\text{g}/\text{m}^3$ ,  $16 \sim 24\%$ ). We recognized that the impacts of anthropogenic drivers on PM<sub>2.5</sub> concentrations in the southern and eastern parts of Zhejiang were evidently weaker than those in other regions in the YRD. This divergence can mostly be explained by spatial distributions of anthropogenic emissions. That is, anthropogenic emissions in the southern and eastern of Zhejiang were also significantly less than those in other regions (Figure S9), thus leading to substantially low PM<sub>2.5</sub> concentrations (Figure 3). Besides, meteorological fields in coastal regions, more conducive to PM<sub>2.5</sub> diffusion (Figure 5), might be another cause. The above findings confirmed that the PM<sub>2.5</sub> mitigation was dominated by anthropogenic emission controls, rather than meteorological variations. Furthermore, the corresponding spatiotemporal patterns were highly correlated to those of the anthropogenic emissions (Figure S9). This indicates that the impacts of the long-term strategies are mainly driven by anthropogenic emission mitigation.

### 3.3 Ambient PM<sub>2.5</sub> mitigation potential

The G20 summit offered a unique and ideal opportunity to clarify the effects of the most stringent emission control measures across the YRD from 2016 to 2019, which could be regarded as the localized PM<sub>2.5</sub> mitigation potential. Figure 7a shows the spatial differences between the constrained and simulated PM<sub>2.5</sub> concentrations, which were extracted from DA\_G20 and NO\_G20, for the period of the G20 summit. Inherent biases remained, primarily attributable to the priori anthropogenic emissions. Their subsequent impacts were then quantified by comparing the discrepancies between the results from two additional experiments (i.e., DA\_CON\_G20 and NO\_CON\_G20) (Figure 7b). More, such impacts were associated with relatively low standard deviations ( $< 5\%$ ), thus presenting a stably spatiotemporal state (Figure S11). This means that such estimations were also suitable for the G20 summit. Therefore, by subtracting them, the re-corrected differences would reflect the actual effects of the most stringent emission control measures for the G20 summit (Figure 7c). Such hotspots with extremely negative values reveal the dramatic PM<sub>2.5</sub> mitigations for these specific locations. The corresponding largest decreases in PM<sub>2.5</sub> concentrations ( $35 \mu\text{g}/\text{m}^3$ , 59%) occurred in Hangzhou and its surrounding areas, as expected. Following Hangzhou, other hotspots with relatively prominent declines also emerged in megacities, especially in Shanghai ( $32 \mu\text{g}/\text{m}^3$ , 51%), Nanjing ( $27 \mu\text{g}/\text{m}^3$ , 55%) and Hefei ( $24 \mu\text{g}/\text{m}^3$ , 44%). This behaviour could be explained by two inferences that: (i) local emission controls

in Hangzhou were projected to be conducted with the maximum execution efficiency compared to those in surrounding regions; (ii) most of the emergency measurements generally targeted the vehicle and industry emissions that are clustered around the urban rather than rural areas.

Compared to the long-term policies from 2016 to 2019, the emergency emission control measures implemented during the G20 Summit achieved more significant decreases in  $\text{PM}_{2.5}$  concentrations ( $17 \mu\text{g}/\text{m}^3$  and 41%) over most of the whole domain, especially in Hangzhou ( $24 \mu\text{g}/\text{m}^3$ , 48%) and Shanghai ( $21 \mu\text{g}/\text{m}^3$ , 45%) (Figure 8). Detailed differences are summarized in Table S6.

To gain the regional  $\text{PM}_{2.5}$  mitigation potential, (i) we first pinpointed the main urban areas of Hangzhou that covered 25 grid cells (Figure S12), in which the most substantial  $\text{PM}_{2.5}$  abatement, i.e., the localized  $\text{PM}_{2.5}$  mitigation potential ( $> 22 \mu\text{g}/\text{m}^3$  and  $> 59\%$ ) were identified. (ii) As the above hypothesis, the spatial distributions of the regional  $\text{PM}_{2.5}$  mitigation potential across the YRD were then assumed to follow those of the long-term strategy effects. (iii) Thus, by extrapolation in equal proportion following such patterns and the localized  $\text{PM}_{2.5}$  mitigation potential, we established the map of the  $\text{PM}_{2.5}$  mitigation potential across the YRD (Figure 9a). It should be noted that, as long as three premises, including typical weather backgrounds, stable structures of anthropogenic emissions, and analogous emission control measures, remain unchanged, Figure 9a is a reliably quantitative reference to characterize the attainable  $\text{PM}_{2.5}$  abatement for the YRD in future.

#### 4 DISCUSSION

The actual effectiveness of anthropogenic emission control measures, especially those directed at  $\text{PM}_{2.5}$  mitigation, has long been excluded from evaluation of air pollution policies in China, in part due to the complex synergy between anthropogenic emissions and meteorology. Here, we provide a novel approach to explore the  $\text{PM}_{2.5}$  responses to anthropogenic emission control measures and their mitigation potential from 2016 to 2019 across the YRD, China. With the data assimilation method, these estimates are projected to be highly reliable due to the sufficient observational constraints. The results demonstrate that long-term anthropogenic emission control strategies from 2016 to 2019 have led to extensive impacts on  $\text{PM}_{2.5}$  abatement across the YRD, especially in the megacities, Shanghai, Hangzhou, Nanjing, and Hefei. In the context of the G20 summit, the emergency strategies could achieve significant  $\text{PM}_{2.5}$  abatement ( $> 50\%$ ) at specific locations, (i.e., urban Hangzhou), representing the localized mitigation potential. By extrapolation based on the above results, we have established the first map of the  $\text{PM}_{2.5}$  mitigation potential for the YRD.

Numerous analyses have focused on Hangzhou during the G20 summit to detect impacts of emergency emission controls (Li et al., 2019b, 2017c; Yu et al., 2018). However, previous analyses generally found more effective predictions ( $> 50\%$ ) at the city level. This discrepancy might be related to the fact that such results were generally based on sole model-dependent predictions, which are normally driven by uncertain bottom-up estimates of anthropogenic emissions. In addition, this study

addresses the YRD after 2016. Besides, similar opportunities also occurred at other spatiotemporal scales, such as the “APEC Blue” in 2014 and “Parade Blue” in 2015 over the BTH (Liu et al., 2016; Sun et al., 2016; Zhang et al., 2016). More aggressive achievements (> 55%) were generally attributed to emergency anthropogenic emission control measures (Sun et al., 2016). This might be related to the fact that, compared to the YRD, the BTH is associated with more abundant primary emissions (Zhang et al., 2019). The impacts of natural sources (e.g., biogenic emissions, wild fires, and natural dust) are not considered in this study. This is mainly because of two reasons. First, it has been widely demonstrated that biogenic emission changes are dominated by meteorological variations over a period of a few years (Wang et al., 2019). Moreover, the former is generally of minor significance for interannual PM<sub>2.5</sub> variations for the YRD (Mu and Liao, 2014; Tai et al., 2012). Second, satellite products, including MOD14 and AIRIBQAP\_NRT.005 (<https://worldview.earthdata.nasa.gov/>), show that there was no noticeable wild fires and natural dust storms during this study period, thus allowing us to ignore the corresponding interferences. This study takes the advantage of observational constraints to gain the regional PM<sub>2.5</sub> mitigation potential. It could be further optimized by more extensive observations. Besides, extending the PM<sub>2.5</sub> mitigation potential in urban Hangzhou during the study period to the entire YRD in other time periods may introduce some uncertainties due to varying meteorology. As abovementioned, impacts of the extreme emergency emission controls are spatially inconsistent across the YRD. To explore regional PM<sub>2.5</sub> mitigation potential, it is thus unavoidable to extrapolate from local to regional scale. The consequent uncertainty mainly relates to the hypothesis that the spatial patterns of the PM<sub>2.5</sub> mitigation potential across the YRD should follow those of the impacts of the long-term emission control strategies. In addition, there are distinct DA methods (Bocquet et al., 2015). It is thus believed that replacing the OI with another DA algorithm would lead to slightly different results. Note that, as previous studies have demonstrated (Cheng et al., 2019; Zhai et al., 2019; Zhong et al., 2018), model uncertainties remain, although we have verified the constrained results. We have supplemented the additional discussions in Sect. 4 for further explanation. For instance, model simulations of aerosol components (e.g., sulfate and nitrate) are still poorly constrained. Moreover, they have not been evaluated due to lack of available observations. Yet previous studies find that the model tends to underestimate sulfate production during high RH and SOA (Li et al., 2017a; Wang et al., 2014; Zhong et al., 2018). As a result, these uncertainties can be propagated into the estimations of meteorological effects. Besides, like other atmospheric chemical transport models, the WRF-CMAQ model cannot provide model uncertainty information, while Monte Carlo simulations for complex CTMs would be unrealistic due to extremely high computation loadings (Zhong et al., 2018). Looking forward, continued advances in observational techniques, better understanding of chemical and meteorological processes, and their improved representations in CTMs are all factors that are critical to optimizing the estimates of the PM<sub>2.5</sub> mitigation potential.

381 **ASSOCIATED CONTENT**

382 **Supporting Information.**

383 The supplement related to this article is available online.

384 **NOTES**

385 The authors declare no competing financial interest.

386 **ACKNOWLEDGEMENTS**

387 This study was supported by the Department of Science and Technology of China (No. 2016YFC0202702, 2018YFC0213506  
388 and 2018YFC0213503), National Research Program for Key Issues in Air Pollution Control in China (No. DQGG0107) and  
389 National Natural Science Foundation of China (No. 21577126 and 41561144004). Pengfei Li is supported by Initiation Fund  
390 for Introducing Talents of Hebei Agricultural University (412201904) and Hebei Youth Top Fund (BJ2020032).

391 **REFERENCES**

392 Adhikary, B., Kulkarni, S., Dallura, A., Tang, Y., Chai, T., Leung, L. R., Qian, Y., Chung, C. E., Ramanathan, V. and  
393 Carmichael, G. R.: A regional scale chemical transport modeling of Asian aerosols with data assimilation of AOD  
394 observations using optimal interpolation technique, *Atmos. Environ.*, 42(37), 8600–8615, 2008.

395 An, Z., Huang, R.-J., Zhang, R., Tie, X., Li, G., Cao, J., Zhou, W., Shi, Z., Han, Y., Gu, Z. and others: Severe haze in  
396 Northern China: A synergy of anthropogenic emissions and atmospheric processes, *Proc. Natl. Acad. Sci.*, 116(18), 8657–  
397 8666, 2019.

398 Binkowski, F. S. and Roselle, S. J.: Models-3 Community Multiscale Air Quality (CMAQ) model aerosol component 1.  
399 Model description, *J. Geophys. Res. Atmos.*, 108(D6), 2003.

400 Bocquet, M., Elbern, H., Eskes, H., Hirtl, M., Žabkar, R., Carmichael, G. R., Flemming, J., Inness, A., Pagowski, M., Pérez  
401 Camacho, J. L. and others: Data assimilation in atmospheric chemistry models: current status and future prospects for coupled  
402 chemistry meteorology models, *Atmos. Chem. Phys.*, 15(10), 5325–5358, 2015.

403 Byun, D. and Schere, K. L.: Review of the governing equations, computational algorithms, and other components of the  
404 Models-3 Community Multiscale Air Quality (CMAQ) modeling system, *Appl. Mech. Rev.*, 59(2), 51–77, 2006.

405 Carlton, A. G. and Baker, K. R.: Photochemical modeling of the Ozark isoprene volcano: MEGAN, BEIS, and their impacts  
406 on air quality predictions, *Environ. Sci. Technol.*, 45(10), 4438–4445, 2011.

407 Carlton, A. G., Bhawe, P. V., Napelenok, S. L., Edney, E. O., Sarwar, G., Pinder, R. W., Pouliot, G. A. and Houyoux, M.:  
 408 Model representation of secondary organic aerosol in CMAQv4. 7, *Environ. Sci. Technol.*, 44(22), 8553–8560, 2010.  
 409 Chai, T., Kim, H.-C., Pan, L., Lee, P. and Tong, D.: Impact of Moderate Resolution Imaging Spectroradiometer Aerosol  
 410 Optical Depth and AirNow PM<sub>2.5</sub> assimilation on Community Multi-scale Air Quality aerosol predictions over the  
 411 contiguous United States, *J. Geophys. Res. Atmos.*, 122(10), 5399–5415, 2017.  
 412 Chen, D., Liu, Z., Ban, J., Zhao, P. and Chen, M.: Retrospective analysis of 2015--2017 wintertime PM<sub>2.5</sub> in China:  
 413 response to emission regulations and the role of meteorology, *Atmos. Chem. Phys.*, 19(11), 7409–7427, 2019.  
 414 Cheng, J., Su, J., Cui, T., Li, X., Dong, X., Sun, F., Yang, Y., Tong, D., Zheng, Y., Li, Y. and others: Dominant role of  
 415 emission reduction in PM<sub>2.5</sub> air quality improvement in Beijing during 2013--2017: A model-based decomposition analysis,  
 416 *Atmos. Chem. Phys.*, 19(9), 6125–6146, 2019.  
 417 Choi, Y.-J. and Fernando, H. J. S.: Implementation of a windblown dust parameterization into MODELS-3/CMAQ:  
 418 Application to episodic PM events in the US/Mexico border, *Atmos. Environ.*, 42(24), 6039–6046, 2008.  
 419 Clough, S. A., Shephard, M. W., Mlawer, E. J., Delamere, J. S., Iacono, M. J., Cady-Pereira, K., Boukabara, S. and Brown,  
 420 P. D.: Atmospheric radiative transfer modeling: a summary of the AER codes, *J. Quant. Spectrosc. Radiat. Transf.*, 91(2),  
 421 233–244, 2005.  
 422 Feng, L. and Liao, W.: Legislation, plans, and policies for prevention and control of air pollution in China: achievements,  
 423 challenges, and improvements, *J. Clean. Prod.*, 112, 1549–1558, 2016.  
 424 Fountoukis, C. and Nenes, A.: ISORROPIA II: a computationally efficient thermodynamic equilibrium model for K<sup>+</sup>--Ca  
 425 2<sup>+</sup>--Mg 2<sup>+</sup>--NH<sub>4</sub><sup>+</sup>--Na<sup>+</sup>--SO<sub>4</sub><sup>2-</sup>--NO<sub>3</sub><sup>-</sup>--Cl<sup>-</sup>--H<sub>2</sub>O aerosols, *Atmos. Chem. Phys.*, 7(17), 4639–4659, 2007.  
 426 Gao, M., Saide, P. E., Xin, J., Wang, Y., Liu, Z., Wang, Y., Wang, Z., Pagowski, M., Guttikunda, S. K. and Carmichael, G.  
 427 R.: Estimates of health impacts and radiative forcing in winter haze in eastern China through constraints of surface PM<sub>2.5</sub>  
 428 predictions, *Environ. Sci. Technol.*, 51(4), 2178–2185, 2017.  
 429 Geng, G., Zhang, Q., Martin, R. V., Lin, J., Huo, H., Zheng, B., Wang, S. and He, K.: Impact of spatial proxies on the  
 430 representation of bottom-up emission inventories: A satellite-based analysis., *Atmos. Chem. Phys.*, 17(6), 2017.  
 431 Hollingsworth, A. and Lönnberg, P.: The statistical structure of short-range forecast errors as determined from radiosonde  
 432 data. Part I: The wind field, *Tellus A*, 38(2), 111–136, 1986.  
 433 Huang, R.-J., Zhang, Y., Bozzetti, C., Ho, K.-F., Cao, J.-J., Han, Y., Daellenbach, K. R., Slowik, J. G., Platt, S. M.,  
 434 Canonaco, F. and others: High secondary aerosol contribution to particulate pollution during haze events in China, *Nature*,  
 435 514(7521), 218, 2014.

436 Ji, Y., Qin, X., Wang, B., Xu, J., Shen, J., Chen, J., Huang, K., Deng, C., Yan, R., Xu, K. and others: Counteractive effects  
 437 of regional transport and emission control on the formation of fine particles: a case study during the Hangzhou G20 summit,  
 438 *Atmos. Chem. Phys.*, 18(18), 13581–13600, 2018.

439 Jiang, Z., McDonald, B. C., Worden, H., Worden, J. R., Miyazaki, K., Qu, Z., Henze, D. K., Jones, D. B. A., Arellano, A. F.,  
 440 Fischer, E. V and others: Unexpected slowdown of US pollutant emission reduction in the past decade, *Proc. Natl. Acad.*  
 441 *Sci.*, 115(20), 5099–5104, 2018.

442 Jung, J., Souri, A. H., Wong, D. C., Lee, S., Jeon, W., Kim, J. and Choi, Y.: The Impact of the Direct Effect of Aerosols on  
 443 Meteorology and Air Quality Using Aerosol Optical Depth Assimilation During the KORUS-AQ Campaign, *J. Geophys.*  
 444 *Res. Atmos.*, 124(14), 8303–8319, 2019.

445 Kain, J. S.: The Kain-Fritsch convective parameterization: an update, *J. Appl. Meteorol.*, 43(1), 170–181, 2004.

446 Kumar, U., De Ridder, K., Lefebvre, W. and Janssen, S.: Data assimilation of surface air pollutants (O<sub>3</sub> and NO<sub>2</sub>) in the  
 447 regional-scale air quality model AURORA, *Atmos. Environ.*, 60, 99–108,  
 448 doi:<https://doi.org/10.1016/j.atmosenv.2012.06.005>, 2012.

449 Li, B., Wang, F., Yin, H. and Li, X.: Mega events and urban air quality improvement: A temporary show?, *J. Clean. Prod.*,  
 450 217, 116–126, 2019a.

451 Li, G., Bei, N., Cao, J., Huang, R., Wu, J., Feng, T., Wang, Y., Liu, S., Zhang, Q., Tie, X. and Molina, L. T.: A possible  
 452 pathway for rapid growth of sulfate during haze days in China, *Atmos. Chem. Phys.*, 17(5), 3301–3316, doi:10.5194/acp-17-  
 453 3301-2017, 2017a.

454 Li, H., Wang, D., Cui, L., Gao, Y., Huo, J., Wang, X., Zhang, Z., Tan, Y., Huang, Y., Cao, J. and others: Characteristics of  
 455 atmospheric PM<sub>2.5</sub> composition during the implementation of stringent pollution control measures in shanghai for the 2016  
 456 G20 summit, *Sci. Total Environ.*, 648, 1121–1129, 2019b.

457 Li, K., Jacob, D. J., Liao, H., Zhu, J., Shah, V., Shen, L., Bates, K. H., Zhang, Q. and Zhai, S.: A two-pollutant strategy for  
 458 improving ozone and particulate air quality in China, *Nat. Geosci.*, 12(11), 906–910, 2019c.

459 Li, M., Zhang, Q., Kurokawa, J., Woo, J.-H., He, K., Lu, Z., Ohara, T., Song, Y., Streets, D. G., Carmichael, G. R. and  
 460 others: MIX: a mosaic Asian anthropogenic emission inventory under the international collaboration framework of the  
 461 MICS-Asia and HTAP, *Atmos. Chem. Phys.*, 17(2), 2017b.

462 Li, P., Wang, L., Guo, P., Yu, S., Mehmood, K., Wang, S., Liu, W., Seinfeld, J. H., Zhang, Y., Wong, D. C. and others: High  
 463 reduction of ozone and particulate matter during the 2016 G-20 summit in Hangzhou by forced emission controls of industry  
 464 and traffic, *Environ. Chem. Lett.*, 15(4), 709–715, 2017c.



465 Li, X., Choi, Y., Czader, B., Roy, A., Kim, H., Lefer, B. and Pan, S.: The impact of observation nudging on simulated  
 466 meteorology and ozone concentrations during DISCOVER-AQ 2013 Texas campaign, *Atmos. Chem. Phys.*, 16(5), 3127–  
 467 3144, 2016.

468 Liu, H., Liu, C., Xie, Z., Li, Y., Huang, X., Wang, S., Xu, J. and Xie, P.: A paradox for air pollution controlling in China  
 469 revealed by “APEC Blue” and “Parade Blue,” *Sci. Rep.*, 6(1), 1–13, 2016.

470 Ma, C., Wang, T., Mizzi, A. P., Anderson, J. L., Zhuang, B., Xie, M. and Wu, R.: Multi-constituent data assimilation with  
 471 WRF-Chem/DART: Potential for adjusting anthropogenic emissions and improving air quality forecasts over eastern China,  
 472 *J. Geophys. Res. Atmos.*, 2019.

473 Ma, Z., Hu, X., Huang, L., Bi, J. and Liu, Y.: Estimating ground-level PM<sub>2.5</sub> in China using satellite remote sensing,  
 474 *Environ. Sci. Technol.*, 48(13), 7436–7444, 2014.

475 Ma, Z., Hu, X., Sayer, A. M., Levy, R., Zhang, Q., Xue, Y., Tong, S., Bi, J., Huang, L. and Liu, Y.: Satellite-based  
 476 spatiotemporal trends in PM<sub>2.5</sub> concentrations: China, 2004–2013, *Environ. Health Perspect.*, 124(2), 184–192, 2015.

477 Morrison, H. and Gettelman, A.: A new two-moment bulk stratiform cloud microphysics scheme in the Community  
 478 Atmosphere Model, version 3 (CAM3). Part I: Description and numerical tests, *J. Clim.*, 21(15), 3642–3659, 2008.

479 Mu, Q. and Liao, H.: Simulation of the interannual variations of aerosols in China: role of variations in meteorological  
 480 parameters, *Atmos. Chem. Phys.*, 14, 11177–11219, 2014.

481 Ni, Z.-Z., Luo, K., Gao, Y., Gao, X., Jiang, F., Huang, C., Fan, J.-R., Fu, J. S. and Chen, C.-H.: Spatial--temporal variations  
 482 and process analysis of  $\text{O}_3$  pollution in Hangzhou during the G20 summit, *Atmos. Chem. Phys.*, 20(10), 5963–  
 483 5976, doi:10.5194/acp-20-5963-2020, 2020.

484 Pleim, J. E.: A combined local and nonlocal closure model for the atmospheric boundary layer. Part I: Model description and  
 485 testing, *J. Appl. Meteorol. Climatol.*, 46(9), 1383–1395, 2007a.

486 Pleim, J. E.: A combined local and nonlocal closure model for the atmospheric boundary layer. Part II: Application and  
 487 evaluation in a mesoscale meteorological model, *J. Appl. Meteorol. Climatol.*, 46(9), 1396–1409, 2007b.

488 RenHe, Z., Li, Q. and Zhang, R.: Meteorological conditions for the persistent severe fog and haze event over eastern China  
 489 in January 2013, *Sci. China Earth Sci.*, 57(1), 26–35, doi:10.1007/s11430-013-4774-3, 2014.

490 Rutherford, I. D.: Data assimilation by statistical interpolation of forecast error fields, *J. Atmos. Sci.*, 29(5), 809–815, 1972.

491 Seinfeld, J. H. and Pandis, S. N.: *Atmospheric chemistry and physics: from air pollution to climate change*, John Wiley &  
 492 Sons., 2016.

493 Sheehan, P., Cheng, E., English, A. and Sun, F.: China’s response to the air pollution shock, *Nat. Clim. Chang.*, 4(5), 306,  
 494 2014.

495 Shi, H., Wang, Y., Chen, J. and Huisinigh, D.: Preventing smog crises in China and globally, *J. Clean. Prod.*, 112, 1261–  
 496 1271, 2016.

497 Shu, L., Wang, T., Han, H., Xie, M., Chen, P., Li, M. and Wu, H.: Summertime ozone pollution in the Yangtze River Delta  
 498 of eastern China during 2013–2017: Synoptic impacts and source apportionment, *Environ. Pollut.*, 113631, 2019.

499 Sun, Y., Wang, Z., Wild, O., Xu, W., Chen, C., Fu, P., Du, W., Zhou, L., Zhang, Q., Han, T. and others: “APEC blue”:  
 500 secondary aerosol reductions from emission controls in Beijing, *Sci. Rep.*, 6, 20668, 2016.

501 Tai, A. P. K., Mickley, L. J. and Jacob, D. J.: Impact of 2000–2050 climate change on fine particulate matter (PM<sub>2.5</sub>) air  
 502 quality inferred from a multi-model analysis of meteorological modes, *Atmos. Chem. Phys.*, 2012.

503 Wang, P., Guo, H., Hu, J., Kota, S. H., Ying, Q. and Zhang, H.: Responses of PM<sub>2.5</sub> and O<sub>3</sub> concentrations to changes of  
 504 meteorology and emissions in China, *Sci. Total Environ.*, 662, 297–306, 2019.

505 Wang, Y., Zhang, Q., Jiang, J., Zhou, W., Wang, B., He, K., Duan, F., Zhang, Q., Philip, S. and Xie, Y.: Enhanced sulfate  
 506 formation during China’s severe winter haze episode in January 2013 missing from current models, *J. Geophys. Res.*  
 507 *Atmos.*, 119(17), 10,410–425,440, doi:10.1002/2013JD021426, 2014.

508 Wong, D. C., Pleim, J., Mathur, R., Binkowski, F., Otte, T., Gilliam, R., Pouliot, G., Xiu, A., Young, J. O. and Kang, D.:  
 509 WRF-CMAQ two-way coupled system with aerosol feedback: software development and preliminary results, *Geosci. Model*  
 510 *Dev.*, 5(2), 299–312, 2012.

511 Xie, H., Wang, L., Ling, X., Miao, Y., Shen, X., Wang, M. and Xin, Y.: China air quality management assessment report  
 512 (2016), 2015.

513 Xiu, A. and Pleim, J. E.: Development of a land surface model. Part I: Application in a mesoscale meteorological model, *J.*  
 514 *Appl. Meteorol.*, 40(2), 192–209, 2001.

515 Xue, T., Zheng, Y., Tong, D., Zheng, B., Li, X., Zhu, T. and Zhang, Q.: Spatiotemporal continuous estimates of PM<sub>2.5</sub>  
 516 concentrations in China, 2000–2016: A machine learning method with inputs from satellites, chemical transport model, and  
 517 ground observations, *Environ. Int.*, 123, 345–357, 2019.

518 Yan, B., Liu, S., Zhao, B., Li, X., Fu, Q. and Jiang, G.: China’s fight for clean air and human health, 2018.

519 Yang, W., Yuan, G. and Han, J.: Is China’s air pollution control policy effective? Evidence from Yangtze River Delta cities,  
 520 *J. Clean. Prod.*, 220, 110–133, 2019.

521 Yang, Y., Liao, H. and Lou, S.: Increase in winter haze over eastern China in recent decades: Roles of variations in  
 522 meteorological parameters and anthropogenic emissions, *J. Geophys. Res. Atmos.*, 121(21), 13,13–50,65,  
 523 doi:10.1002/2016JD025136, 2016.

524 Yarwood, G., Rao, S., Yocke, M. and Whitten, G. Z.: Updates to the carbon bond chemical mechanism: CB05, Final Rep. to  
 525 US EPA, RT-0400675, 8, 2005.

526 Yu, H., Dai, W., Ren, L., Liu, D., Yan, X., Xiao, H., He, J. and Xu, H.: The effect of emission control on the submicron  
 527 particulate matter size distribution in Hangzhou during the 2016 G20 Summit, *Aerosol Air Qual. Res.*, 18, 2038–2046, 2018.  
 528 Yu, S., Mathur, R., Pleim, J., Wong, D., Gilliam, R., Alapaty, K., Zhao, C. and Liu, X.: Aerosol indirect effect on the grid-  
 529 scale clouds in the two-way coupled WRF-CMAQ: model description, development, evaluation and regional analysis,  
 530 *Atmos. Chem. Phys. Discuss.*, 25649, 2013.  
 531 Zhai, S., Jacob, D. J., Wang, X., Shen, L., Li, K., Zhang, Y., Gui, K., Zhao, T. and Liao, H.: Fine particulate matter (PM<sub>2.5</sub>)  
 532 trends in China, 2013–2018: separating contributions from anthropogenic emissions and meteorology, *Atmos. Chem. Phys.*,  
 533 19(16), 11031–11041, doi:10.5194/acp-19-11031-2019, 2019.  
 534 Zhang, L., Shao, J., Lu, X., Zhao, Y., Hu, Y., Henze, D. K., Liao, H., Gong, S. and Zhang, Q.: Sources and processes  
 535 affecting fine particulate matter pollution over North China: an adjoint analysis of the Beijing APEC period, *Environ. Sci.*  
 536 *Technol.*, 50(16), 8731–8740, 2016.  
 537 Zhang, Q., He, K. and Huo, H.: Policy: cleaning China’s air, *Nature*, 484(7393), 161, 2012.  
 538 Zhang, Q., Zheng, Y., Tong, D., Shao, M., Wang, S., Zhang, Y., Xu, X., Wang, J., He, H., Liu, W. and others: Drivers of  
 539 improved PM<sub>2.5</sub> air quality in China from 2013 to 2017, *Proc. Natl. Acad. Sci.*, 2019.  
 540 Zhang, R., Wang, G., Guo, S., Zamora, M. L., Ying, Q., Lin, Y., Wang, W., Hu, M. and Wang, Y.: Formation of urban fine  
 541 particulate matter, *Chem. Rev.*, 115(10), 3803–3855, 2015.  
 542 Zhang, Y.-L. and Cao, F.: Fine particulate matter (PM<sub>2.5</sub>) in China at a city level, *Sci. Rep.*, 5, 14884, 2015.  
 543 Zhong, Q., Ma, J., Shen, G., Shen, H., Zhu, X., Yun, X., Meng, W., Cheng, H., Liu, J., Li, B., Wang, X., Zeng, E. Y., Guan,  
 544 D. and Tao, S.: Distinguishing Emission-Associated Ambient Air PM<sub>2.5</sub> Concentrations and Meteorological Factor-Induced  
 545 Fluctuations, *Environ. Sci. Technol.*, 52(18), 10416–10425, doi:10.1021/acs.est.8b02685, 2018.  
 546

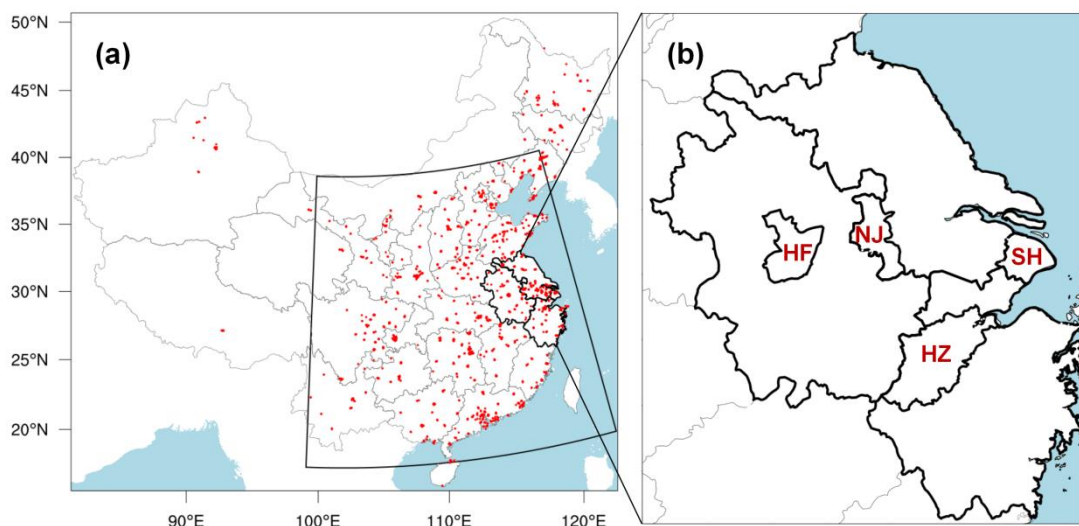


**Figure 1. (a) The model domain. Red dots denote the ground-level PM<sub>2.5</sub> measurements, which, within the fan-shaped quadrilateral, are used to constrain the model predictions. (b) Black lines outline the boundaries of the Yangtze River Delta (YRD), as well as four major cities considered (i.e., SH: Shanghai; HZ: Hangzhou; NJ: Nanjing; HF: Hefei).**

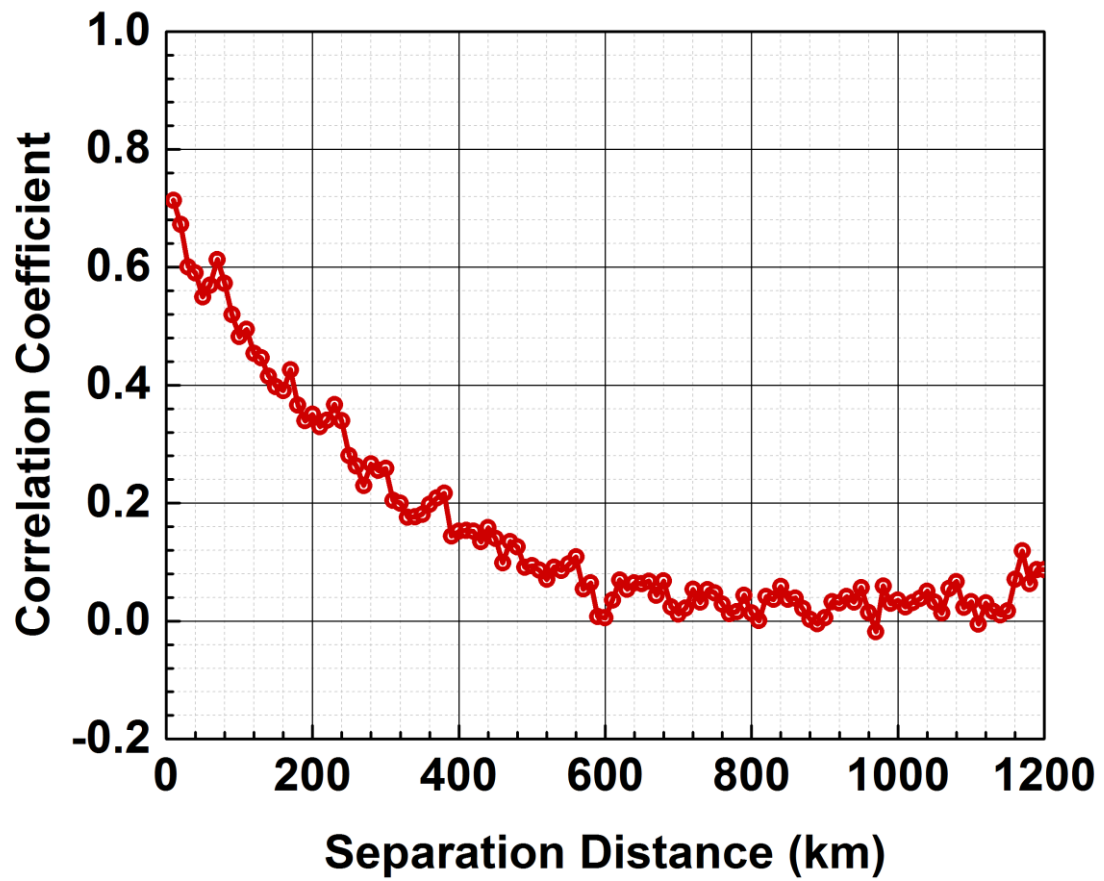


Figure 2. Correlation coefficients (averaged over 10 km) as a function of the separation distances between two surface-level monitoring stations using the Hollingsworth-Lönnerberg method.

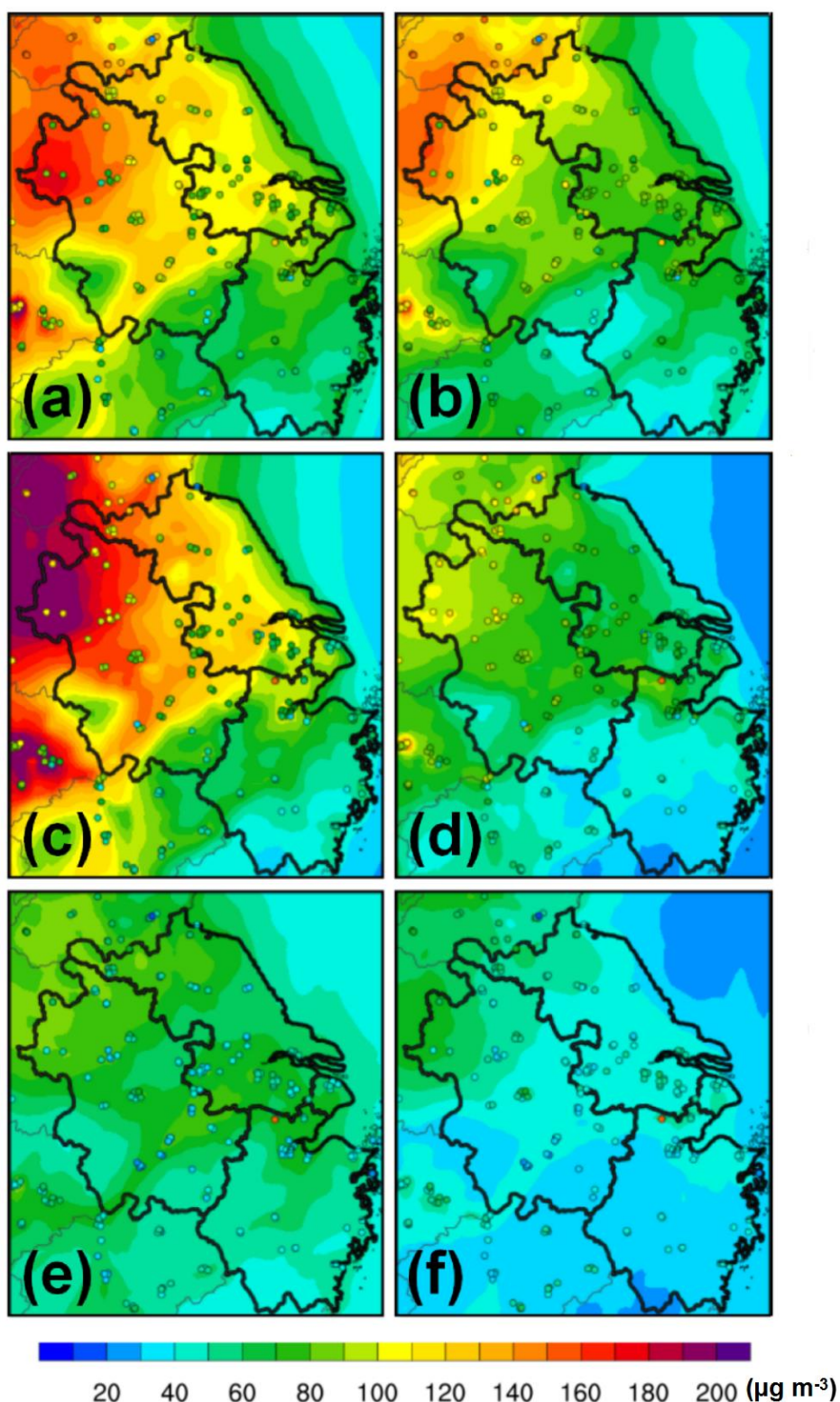


Figure 3. Spatial comparisons of hourly-averaged concentrations of simulated and constrained PM<sub>2.5</sub> with surface observations across the YRD for January 2016 (top panel), January 2019 (middle panel), and the G20 summit (bottom panel): (a) NO\_2016; (b) DA\_2016; (c) NO\_2019; (d) DA\_2019; (e) NO\_G20; (f) DA\_G20. Circles denote ground measurement sites.

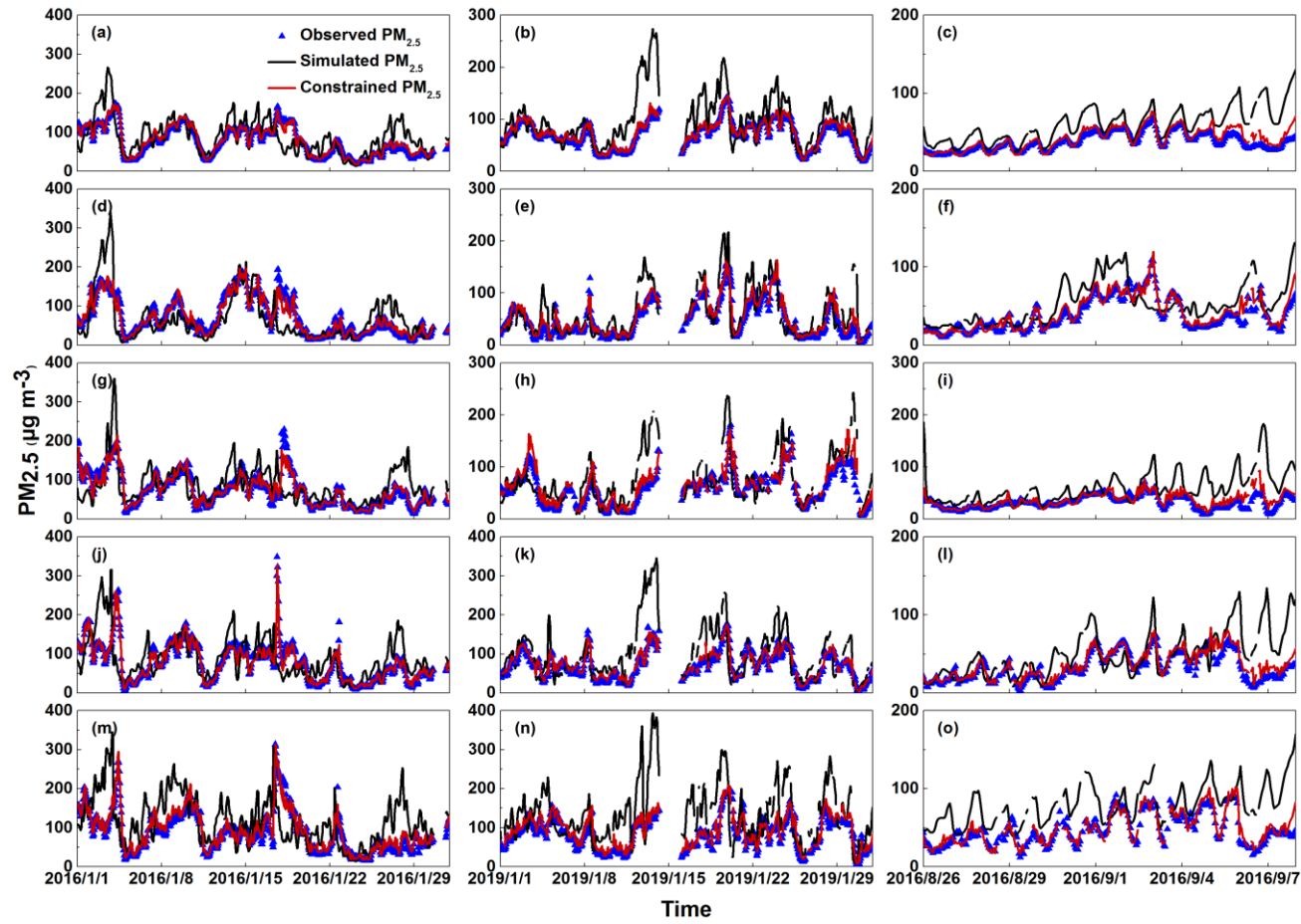


Figure 4. Time series of the comparisons between hourly observed, simulated, and constrained PM<sub>2.5</sub> concentrations for January 2016 (left column), January 2019 (middle column), and the G20 summit (right column) over (a – c) the whole domain as well as in four representative cities, which are as follows: (d - f) Shanghai, (g - i) Hangzhou, (j - l) Nanjing, and (m - o) Hefei. The black circles, black lines, and red lines denote the hourly observed, simulated, and constrained PM<sub>2.5</sub> concentrations, respectively.



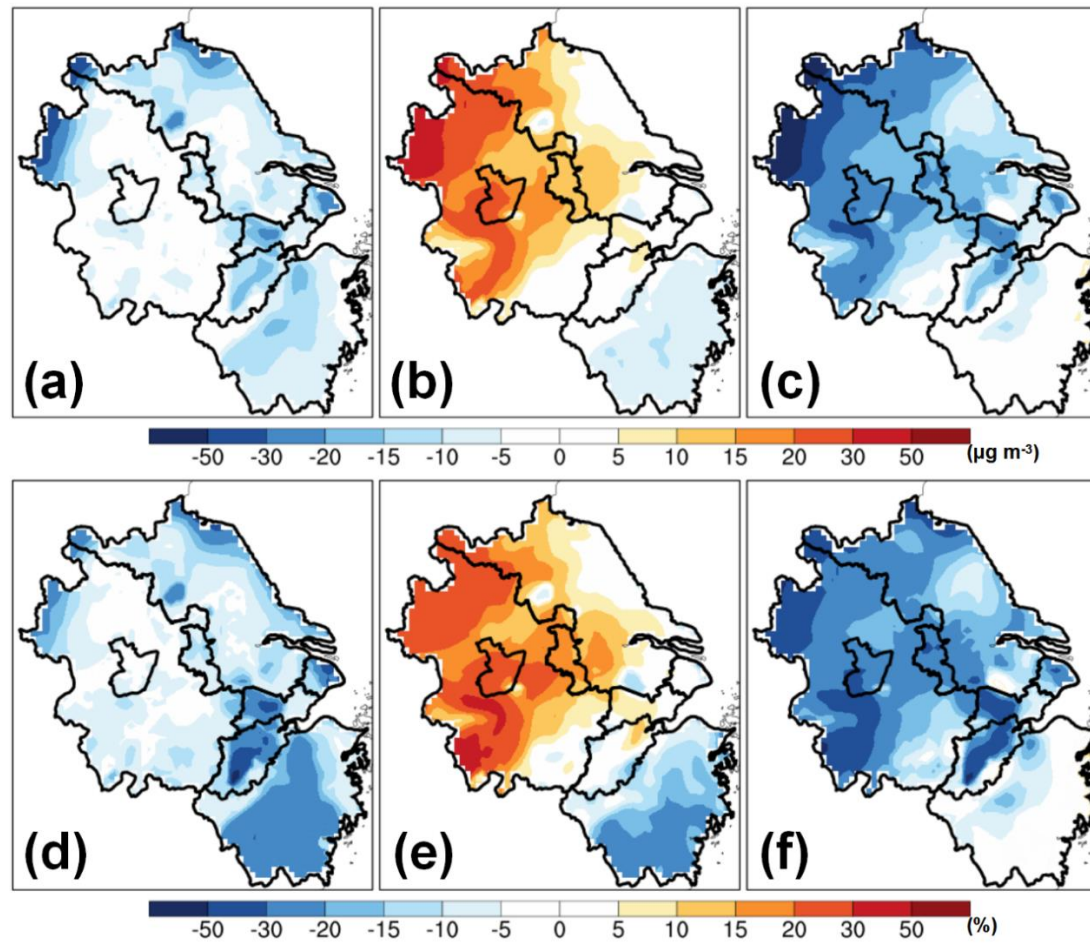
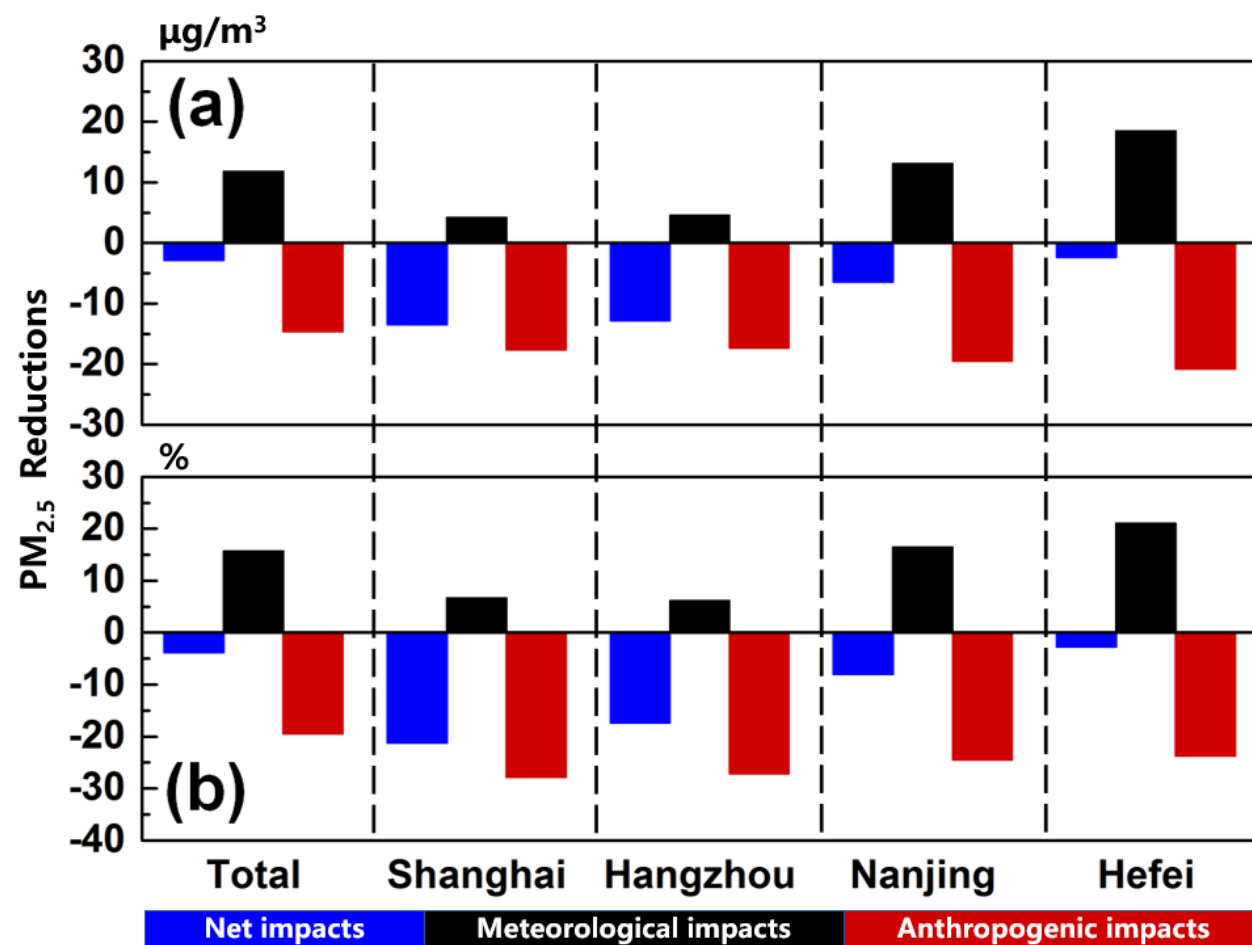


Figure 5. The impacts of anthropogenic emission controls and meteorological variations on spatial PM<sub>2.5</sub> concentrations in January from 2016 to 2019. (a, d) Their net impacts. (b, e) meteorological impacts. (c, f) the impacts of anthropogenic emission controls. The top and bottom panels refer to the changes in absolute values and relative percentages, respectively.



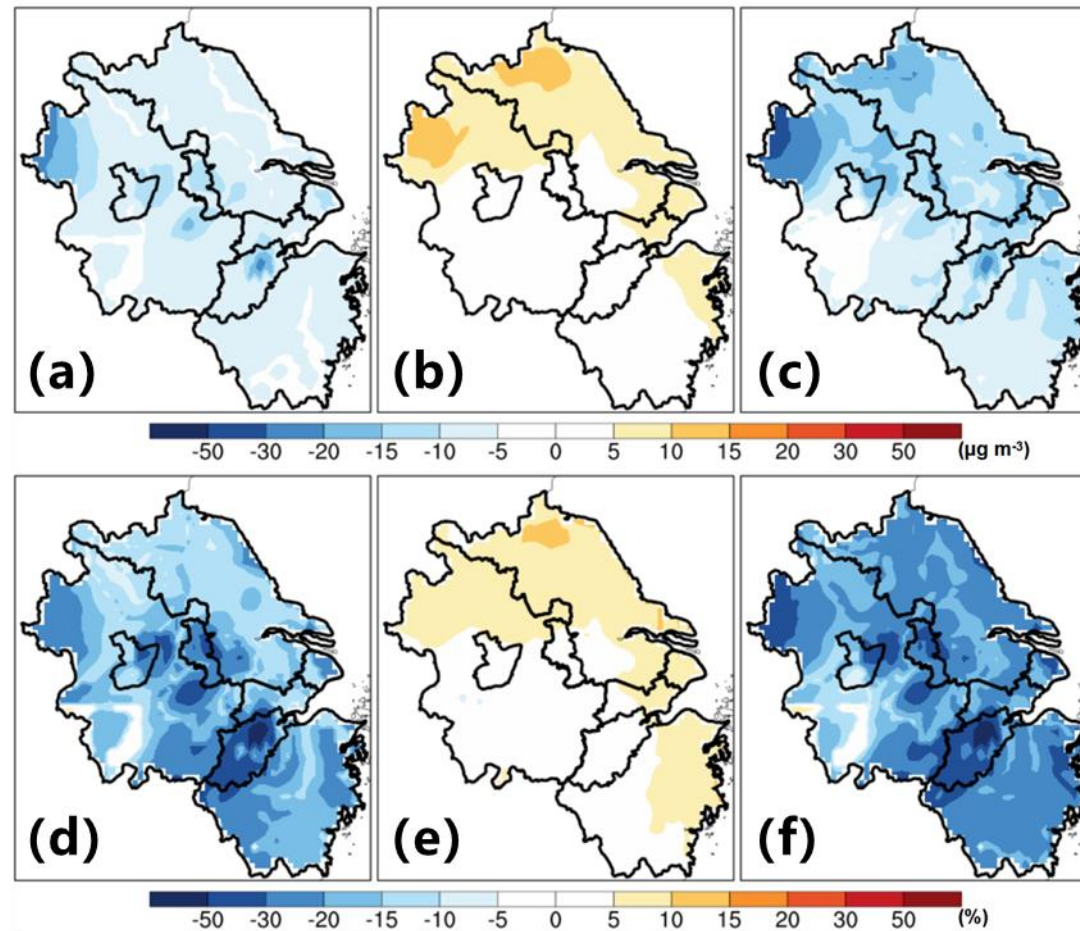


527

528

529

Figure 6. The impacts of anthropogenic emission controls and meteorological variations on PM<sub>2.5</sub> concentrations in January from 2016 to 2019 over the whole domain as well as in four representative cities (i.e., Shanghai, Hangzhou, Nanjing, and Hefei). The top and bottom panels refer to the changes in absolute values and relative percentages, respectively.



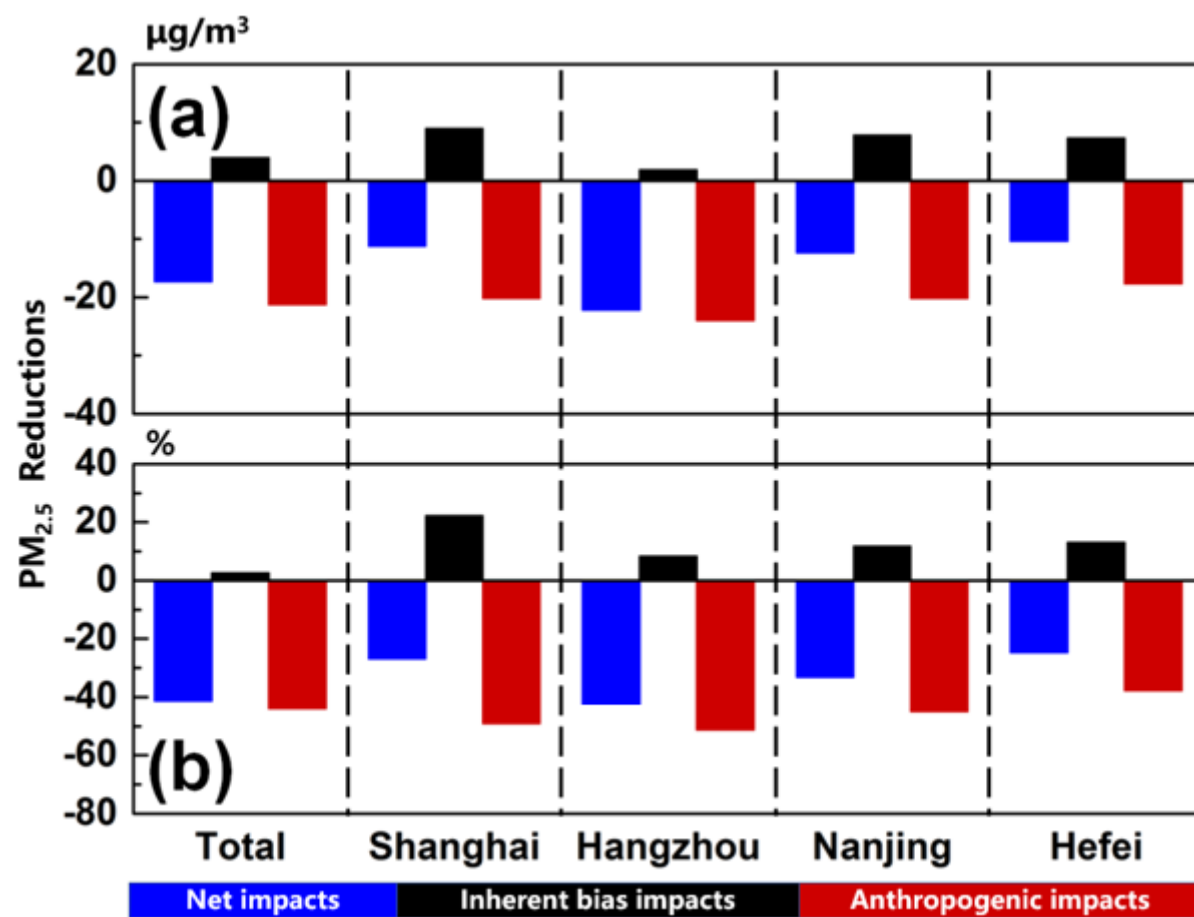
530

531

532

533

Figure 7. The impacts of anthropogenic emission controls and inherent biases on spatial PM<sub>2.5</sub> concentrations during the G20 summit. (a, d) Their net impacts. (b, e) the impacts of inherent biases. (c, f) the impacts of anthropogenic emission controls. The top and bottom panels refer to the changes in absolute values and relative percentages, respectively. Inherent biases are mainly due to the prior anthropogenic emissions.



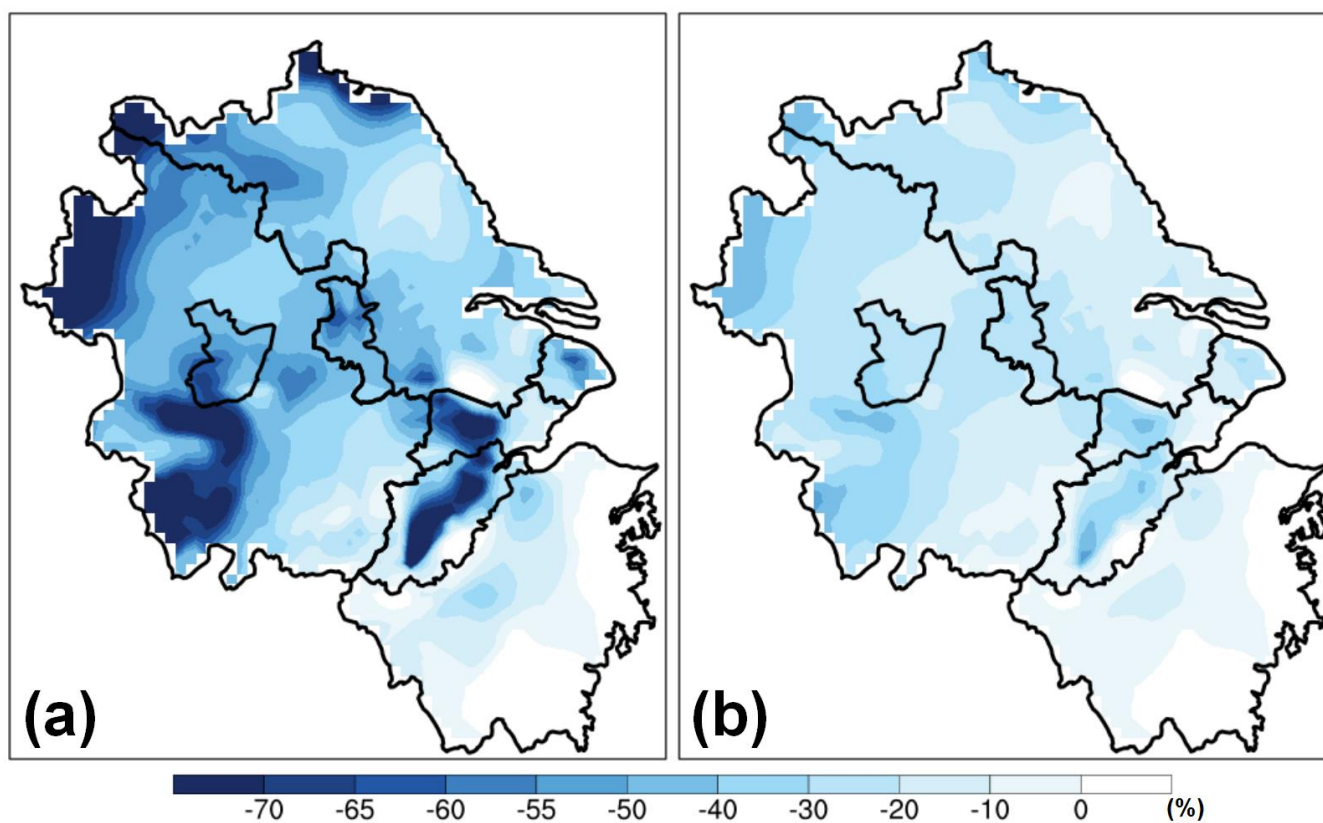
534

535

536

537

Figure 8. The impacts of anthropogenic emission controls and inherent biases on PM<sub>2.5</sub> concentrations during the G20 summit over the whole domain as well as in four representative cities (i.e., Shanghai, Hangzhou, Nanjing, and Hefei). The top and bottom panels refer to the changes in absolute values and relative percentages, respectively. Inherent biases are mainly due to the prior anthropogenic emissions.



538

539 Figure 9. (a) Spatial distributions of the PM<sub>2.5</sub> mitigation potential across the YRD and (b) their differences with the impacts of long-term emission control strategies from 2016 to 2019  
 540 (Fig. 5f). Both spatial patterns of long-term emission control strategy impacts (Fig. 5f) and the localized PM<sub>2.5</sub> mitigation potential in the main urban areas of Hangzhou (Fig. S10), with  
 541 the proportion calculator, result in Fig. 9a.

542

543

**Table 1. The experiments to isolate the effects of anthropogenic emission controls due to the long-term and emergency emission control strategies.**

| Experiments | Time Periods  | Priori Anthropogenic Emissions | Constrained Meteorology | Constrained Observations | Comparisons and Purposes  |
|-------------|---|--------------------------------|-------------------------|--------------------------|---|
| DA_2016     | January 2016  | MEICv1.2                       | Yes                     | Yes                      | The net effects of major driving factors (i.e., anthropogenic emission controls and meteorological variations) from 2016 to 2019.                                   |
| DA_2019     | January 2019  |                                | Yes                     | Yes                      |   |
| NO_2016     | January 2016  | MEICv1.2                       | Yes                     | No                       | The effects of meteorological variations from 2016 to 2019.   |
| NO_2019     | January 2019  |                                | Yes                     | No                       |   |
| DA_G20      | from August 26 to September 7, 2016                                     | MEICv1.2                       | Yes                     | Yes                      | The net effects of major driving factors (i.e., anthropogenic emission controls and the uncertainties in the priori anthropogenic emissions) during the G20 summit. |
| NO_G20      |   |                                | Yes                     | No                       |   |
| DA_CON_G20  | from August 11 to August 23 and from September 18 to September 30, 2016 | MEICv1.2                       | Yes                     | Yes                      | The effects of the uncertainties in the priori anthropogenic emissions.   |
| NO_CON_G20  |   |                                | Yes                     | No                       |   |